Exp Fluids (2012) 53:731–746
DOI 10.1007/s00348-012-1323-3

RESEARCH ARTICLE

# Pre- and post-injection flow characterization in a heavy-duty diesel engine using high-speed PIV

**R. P. C. Zegers · C. C. M. Luijten · N. J. Dam · L. P. H. de Goey**

Received: 7 September 2011 / Revised: 17 April 2012 / Accepted: 18 May 2012 / Published online: 5 June 2012


**Abstract** High-speed particle image velocimetry (HS-PIV) using hollow microspheres has been applied to characterize the flow in a heavy-duty diesel engine during and after fuel injection. The injection timings were varied in the range representing those used in premixed charge compression ignition (PCCI) regimes, and multiple injections have been applied to investigate their influence on the flow inside the combustion chamber. By injecting into pure nitrogen, combustion is avoided and the flow can be studied long after injection. The results show a sudden change of air motion at the start of injection as a result of the air entrainment at the core of the spray. Furthermore, as expected, spray injection causes a considerable increase in the cycle-to-cycle fluctuations of the flow pattern, the more so for longer injection durations.

## 1 Introduction

Due to stringent emission legislation, there is widespread interest in alternative combustion strategies for internal combustion engines. One of these new strategies is the combination of the Otto and Diesel principles, the so-called premixed charge compression ignition (PCCI) concept. This strategy involves a certain amount of premixing of fuel and air inside the engine prior to ignition. The exact amount of pre-mixing is crucial for combustion behavior and emission formation. Premixing occurs in the ignition delay (ID) period, which is defined as the time between start of injection (SOI) and the start of combustion (SOC). When a diesel engine is operated in PCCI mode, the ignition delay is (much) larger as compared to conventional diesel combustion and larger than ten crank angle degrees (CAD) as shown by Leermakers et al. (2011). Currently, injection pressures in heavy-duty diesel engines of up to 2,500 bar, combined with a long ignition delay, improve the mixing of fuel and air prior to combustion. The influence of the global air flow in the cylinder on the mixing process is of particular interest. Due to the high momentum of the spray, direct injection of a diesel fuel is expected to have a stronger influence on the mixing process than the swirl motion that may or may not be present before injection.

A novel method to investigate pre-mixing during the ignition delay period in PCCI engines is to visualize in-cylinder flows using high-speed particle image velocimetry (HS-PIV). In some cases, the recording speed is fast enough to resolve a large part of the time scales present and can therefore be called time-resolved PIV (TR-PIV). During compression, Cosadia et al. (2007) showed time-resolved results with a recording speed of 1 kHz. PIV has already proven its applicability for visualization of in-cylinder flows in spark ignition and compression ignition engines.

Combustion occurring in spark ignition (SI) engines is influenced by the in-cylinder flow, mostly the tumble motion, and is also very prone to cycle-to-cycle variations. Therefore, PIV measurements in spark ignition engines have focused on understanding the influence of cycle-to-cycle variations on combustion behavior and the occurrence of misfires. Recently, Müller et al. (2010), Peterson and Sick (2009) and Krishna and Mallikarjuna (2010) showed the applicability of (HS-)PIV near the spark plug

R. P. C. Zegers (✉) · C. C. M. Luijten · N. J. Dam · L. P. H. de Goey
Combustion Technology Section, Department of Mechanical Engineering, Eindhoven University of Technology, Eindhoven, The Netherlands
e-mail: r.p.c.zegers@tue.nl
URL: www.combustion.tue.nl

region in SI engines. PIV measurements in a light-duty diesel engine with a typical production piston with re-entrant shape and valve cutout geometries were presented by Petersen and Miles (2011) and Yu et al. (2006). The optical distortion observed through the curved surfaces of the fused silica piston bowl was successfully corrected. Qualitative comparison of PIV with large eddy simulation (LES) data has been presented by Yu et al. (2006). Fuel injection phenomena in a gasoline direct injection (GDI) engine was investigated using PIV by Ekenberg et al. (2001) by injecting compressed air through the gasoline injector.

Diesel sprays in compression ignition engines are influenced by the main swirl, which deflects the sprays away from the central spray axis. This deflection was investigated experimentally and numerically using computational fluid dynamics (CFD) models of spray injection by Dempsey and Reitz (2011). The cyclic variations present in a diesel engine were investigated by Cosadia et al. (2006), who show that the structure of the swirling flow varies significantly from cycle to cycle. The velocity profiles of diesel sprays have been investigated extensively by Hillamo et al. (2008), showing the possibility of measuring the velocity inside a relatively dense diesel spray. The air entrainment and the interaction of multiple sprays were studied by Malbec and Bruneaux (2010), who show a dependence of air entrainment on the distance between two neighboring jets. The interaction of a diesel spray with the flow present in the piston bowl of a heavy-duty Diesel has been visualized by Hillamo et al. (2011). However, a quantification of the spray influence was not included.

The combination of velocity measurements and fuel injection to investigate the velocity field influence after injection is, to the authors knowledge, lacking in literature. Therefore, the effect of fuel injection on the mixing during the ignition delay prior to combustion is still unknown and will be studied in this paper. In previous research of Zegers et al. (2009), flow characteristics at different engine velocities and intake pressures were shown and a linear relation between engine speed and magnitude of in-plane velocity was found. The experiments presented in the present paper were designed to assess the flow during the complete compression cycle, specifically including the injection event and the ignition delay period.

The influence of single and multiple fuel injections is investigated by varying the start of injection timing, common rail pressure and injection duration in ranges, which are representative of PCCI combustion regimes.

In Sect. 2, the experimental engine, high-speed PIV setup and processing steps will be presented, followed by the details of two experimental datasets (with and without fuel injection) and the used analysis methods including proper orthogonal decomposition (POD). The results are presented for the two different datasets in Sect. 3, followed by the conclusions in Sect. 4.

## 2 Methods

### 2.1 Experimental setup

The experimental setup consists of an optically accessible engine and a high-speed PIV setup, described in more detail in the next two subsections.

#### *2.1.1 Optically accessible engine*

The test setup consists of a one-cylinder optically accessible heavy-duty Diesel engine, based on a Ricardo Proteus block and equipped with a DAF MX cylinder head. The engine is driven by an electrical motor. A cross-section of the engine setup is shown in Fig. 1. The piston is elongated, and the upper part of the liner and the piston bottom are both made of sapphire. Via an oval aluminum coated mirror (Molenaar Optics), positioned under 45 degrees, optical access to the combustion chamber is obtained. The hydraulic cylinder can be lowered, allowing easy access to the combustion chamber for cleaning. For details of the engine, we refer to the work of Doosje (2010). The engine specifications are summarized in Table 1.

The engine is equipped with a common rail injector of Delphi Diesel Systems, which can be used up to 2,500 bar injection pressure with up to five injections per cycle. Details are presented in Table 2. To avoid massive light scattering by the injected liquid fuel, n-heptane is chosen instead of diesel. Because of faster vaporization, n-heptane fuel sprays show only a relatively short liquid core.

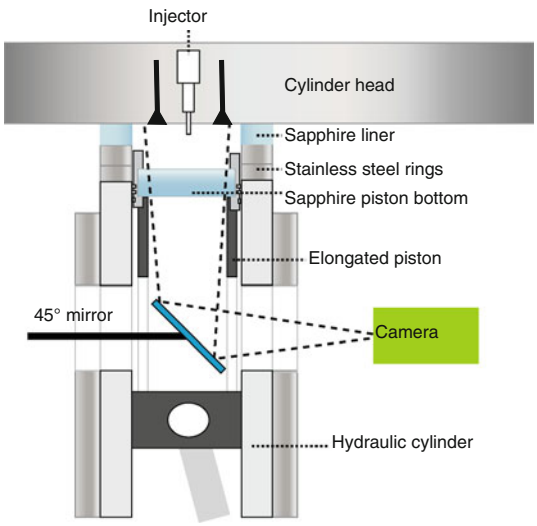


**Fig. 1** Cross-section of the optically accessible engine

**Table 1** Engine specifications (top dead center (TDC) is defined as 360 CAD)

| | |
|---|---|
| Bore | 130 mm |
| Stroke | 156 mm |
| Connecting rod | 270 mm |
| Displacement volume | 2.07 l |
| Compression ratio | 13.9 |
| IVO | 715 CAD |
| IVC | 190 CAD |
| EVO | 500 CAD |
| EVC | 10 CAD |
| Piston bowl/crown | Flat bathtub |
| Piston bowl diameter | 90 mm |
| Piston bowl depth | 20 mm |

*IVO* inlet valve opening, *IVC* inlet valve closing, *EVO* exhaust valve opening, *EVC* exhaust valve closing

**Table 2** Injector specifications

| | |
|---|---|
| Holes | 7 |
| Hole size | 195 μm |
| Flow (nominal) | 1.7 l/min |
| Spray cone angle ($\phi$) | 143 degrees |

Nominal flow is measured by Delphi Diesel systems at 100 bar

### 2.1.2 High-speed PIV setup

The HS-PIV setup consists of an EdgeWave IS8II-DE double-cavity high-speed Nd:YAG laser and a Vision Research Phantom V7.1 high-speed CMOS camera, triggered by a LaVision high-speed controller and DaVis software. The laser has a repetition rate up to 10 kHz and a pulse energy of 7 mJ at 3 kHz. The high-speed camera has a frame rate of 4.8 kHz at full resolution of 800 × 600 pixels. For HS-PIV experiments, the frame straddling technique is used, where one cavity is fired at the end of a certain frame and the other cavity at the beginning of the next frame. This technique reduces the maximum effective frame rate for PIV to 2.4 kHz at full resolution. The laser sheet has a thickness of approximately 1 mm in the engine, and the delay between the two laser pulses is 50 μs.

When performing HS-PIV measurements of relatively large areas, the high-speed laser intensity is too low to achieve enough scattering using regular seeding particles, such as silicon oil droplets of 1 μm. Therefore, relatively large dry-expanded hollow polymer microspheres (Expancel 920 DE40 D30) are used as seeding material. The diameter of the microspheres is $d_p = 40$ μm, and their density is approximately $\rho_p = 30$ kg/m$^3$. The microspheres are seeded using a home-built cyclone that is operated by applying a pressure difference between the intake manifold and the cyclone inlet of 0.2 bar. They are easily seeded into the intake air and do not have any negative influence on the engine behavior, but cleaning of the intake manifold, piston rings, cylinder head and piston is necessary after a few measurements. A similar kind of approach using microspheres can be found in the papers by Towers and Towers (2004), Ekenberg et al. (2001) and Nordgren et al. (2003).

The density ratio between the microspheres and the air at TDC with an intake pressure of 2 bar is $s = 1.07$, reducing the difference between the air and particle velocity. The flow fluctuations that can be followed by the particle are determined by using the approach published by Melling (1997).

The relaxation time (response) of the particles at TDC (800 K) is calculated using $\tau_p = d_p^2 \rho_p / 18\mu$ with a dynamic viscosity of $\mu = 187 \times 10^{-6}$ kg/ms. This results in $\tau_p = 1.4 \times 10^{-5}$ s. An approximation of the characteristic resolved flow scale near the spray is given by $\tau_f = \Delta / V_{\text{spray}}$ where the spatial resolution $\Delta = 10^{-2}$ m and a characteristic spray velocity $V_{\text{spray}} = 100$ m/s resulting in $\tau_f = 10^{-4}$ s. The resulting Stokes number is $S_k = \tau_p / \tau_f = 0.14$, providing acceptable flow tracing accuracy (Melling 1997).

All measurements were carried out at 600 rpm with a resolution of one CAD, resulting in a measurement frequency of 3.6 kHz and a camera frequency of 7.2 kHz. During the compression, this recording speed is appropriate to resolve flow time scales of interest. However, during fuel injection, time scales are much shorter, and therefore, only the large-scale fluctuations are captured. This recording frequency limits the camera resolution to 512 × 512 pixels. When recording the whole field of view, the resolution is 0.16 mm per pixel. The pulse separation is determined to be 50 μs to get an appropriate displacement for in-cylinder flows of around 10 m/s. On average, the particle image size is 2 pixels, corresponding to 0.32 mm. The lowest displacement visible (sub-pixel accuracy) of 0.1 pixels corresponds to 0.32 m/s given the 50 μs pulse separation.

The recorded plane is positioned only two millimeter below the cylinder head to enable the lasersheet to enter the combustion chamber during the whole compression stroke. A detailed representation of the piston position at several crank angle positions is shown in Fig. 2. Obviously, the desire to record data during the passage of the piston through TDC limits the probe volume to the uppermost part of the combustion chamber. The probe volume is also limited by the size of the optical part of the piston bowl resulting in a field of view with a diameter of 8 cm. In particular, no direct information is obtained from the flow fields within the piston bowl or velocities in the vertical plane. Using a completely transparent bowl, for instance as used by Cosadia et al. (2007), Chartier et al. (2011) and Petersen and Miles (2011), might further improve the

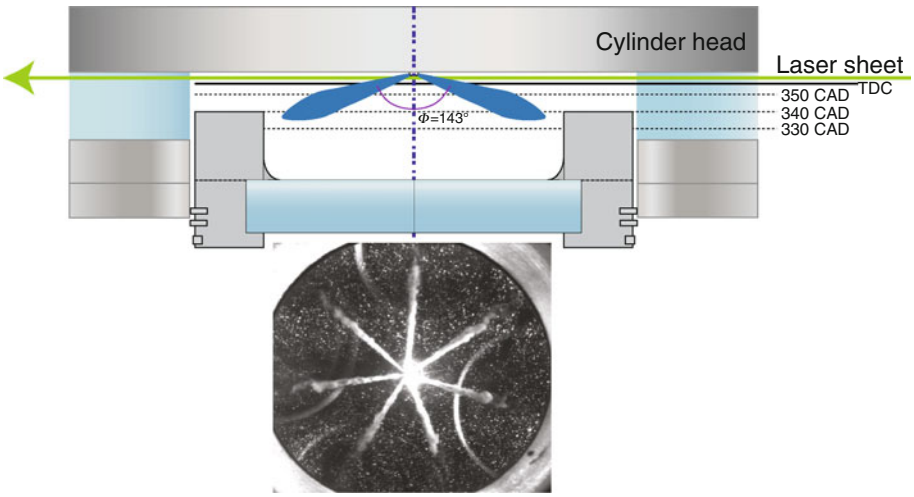


**Fig. 2** Schematic representation of the time-resolved PIV setup during injection via the injector with a spray angle of 143 degrees. The *dotted lines* represent the position of the *upper* rim of the piston at specific CA during the compression stroke. The *black solid line* represents *top* dead center (360 CAD, TDC)

knowledge on the influence of spray injections on the flow fields and therefore the mixing.

*2.1.2.1 Pre-processing parameters* Due to the large scattering efficiency of the microspheres, only minor pre-processing is needed. We normalize the particle intensity by applying a min-max filter with a scale length of 6 pixels. This increases the contrast between the particles and the background. A mask is applied to exclude the edges of the field of view (FOV). After pre-processing, the valve seats can still be seen in the image due to overexposure. The scattering of the fuel spray is reduced by the pre-processing, thereby lowering the error in cross-correlating.

*2.1.2.2 Interrogation parameters* The chosen interrogation parameters represent a trade-off between relatively low velocities prior to injection and the much higher velocities during and after injection. During fuel injection, velocities increase tremendously, and combined with a 50-μs inter-frame time, a relatively coarse grid is needed. The multipass/multigrid scheme used is explained by Raffel et al. (2007). We use sizes of 128 pixels and 64 pixels, with 75 % overlap to increase the spatial-sampling frequency, resulting in an overall spatial resolution of 10.4 mm with a spatial grid spacing of 2.6 mm between each vector. This spatial resolution is two times lower than in the time-resolved PIV study by Cosadia et al. (2007). Using the post-processing values as defined in the next paragraph, maximally 28 % of the 850 calculated vectors were rejected when injecting multiple times. This can be attributed to high out-of-plane velocities. Using a grid size of 32 pixels during interrogation results in a slightly higher amount of rejected vectors than with a 64 pixels grid size. The combination of a bad laser profile and multiple injections resulted in maximally 35 % outliers. To achieve the highest accuracy, spatial resolution has been sacrificed.

*2.1.2.3 Post-processing parameters* Post-processing is applied after each interrogation pass of the multipass/multigrid scheme and after the last pass. A correlation peak height ratio of 1.5 is used to reject spurious vectors, and the vector field is median-filtered by removing vectors that are two times larger than the rms value of their neighbors and only re-inserted when the value was smaller than 3 times the rms value. The resulting velocity field is smoothed using a 3 × 3 filter.

## 2.2 Experimental datasets

The experiments are split in two datasets: without (1) and with (2) fuel injection.

*Dataset 1* The first dataset is used to investigate the statistics of cycle-to-cycle fluctuations without fuel injection. This dataset contains three measurement series of 10 CAD duration (320–329 CAD) and a total of 310 cycles. The intake pressure was kept at 100 kPa.

*Dataset 2* The second dataset comprises 11 cases of 140 CAD duration (260–339 CAD) and 9 cycles each, with injection of n-heptane in pure nitrogen to avoid combustion. The intake pressure was raised to 200 kPa to reduce the liquid spray volume and therefore overexposure of the camera.

An overview of all cases with varying injection pressures, timings and durations is given in Table 3. From this dataset, 8 cases are combined to calculate phase-averaged velocity fields of 72 cycles up to the start of injection (260–330 CAD). The n-heptane injections are split into a maximum of 5 injections during a cycle. Various injection pressures, timings and durations are investigated. The injection durations range from 1 ms up to 6 ms (3 × 2 ms) to represent the full engine load range. As the injection durations are kept constant, the injection amount increases with increasing injection pressure. Varying common rail pressure as a result of previous injections is not taken into account.

**Table 3** Dataset 2: Injection timings (topline) and durations (table entries) for all injection cases studied

| Case | Pressure (bar) | Injection timings and duration (ms) | | | | |
|---|---|---|---|---|---|---|
| | | 310 CAD | 320 CAD | 330 CAD | 340 CAD | 350 CAD |
| 1 | 1,500 | – | – | 1 | 1 | 1 |
| 2 | 1,500 | – | – | – | 1 | – |
| 3 | 2,000 | 1 | 1 | 1 | 1 | 1 |
| 4 | 2,000 | – | – | 1 | 1 | 1 |
| 5 | 2,500 | – | – | 1 | 1 | 1 |
| 6 | 2,500 | – | – | – | – | 3 |
| 7 | 2,500 | – | – | – | 2 | 2 |
| 8 | 2,500 | – | – | 2 | 2 | – |
| 9 | 2,500 | 2 | – | 2 | – | 2 |
| 10 | 2,500 | – | – | – | 3 | – |
| 11 | 2,500 | 1 | 1 | 1 | 1 | 1 |

The low number of cycles prohibits the calculation of a statistically converged phase-averaged velocity field, even though flow analysis can still be performed.

## 2.3 Analysis methods

As mentioned in the introduction, (HS-)PIV results can be used for qualitative comparison with CFD results as shown by Yu et al. (2006). To be able to make this comparison quantitative, proper orthogonal decomposition (POD) is a promising tool to compare LES and PIV data as shown by Meyer et al. (2007). The POD technique and its implementation are briefly introduced below.

### *2.3.1 Proper orthogonal decomposition*

POD is a mathematical technique used to obtain low-dimensional approximate descriptions of high-dimensional processes or to extract main modes from experimental data (see Chatterjee 2000). The basis functions used are orthonormal and ordered such that a combination of the first few functions gives the best possible reconstruction. For POD on velocity fields, the basis functions are themselves velocity fields, and most of the structure in the measured velocity field can be captured by a linear combination of only a few basis functions. In this case, we use the snapshot approach, developed by Sirovich (1987), which is more convenient when the number of collected samples is smaller than the space discretization, according to Bizon et al. (2010). The snapshot approach has been applied in engine flow research to extract coherent structures from a turbulent flow in an unbiased way by Druault et al. (2005) and Roudnitzky et al. (2006) and also for decomposition of soot luminosity during combustion by Bizon et al. (2009). POD has been applied to LES data of a piston-cylinder assembly by Liu and Haworth (2011). The POD, in this case an eigenvalue decomposition, can be performed in a few steps that are explained below, following the strategy of Meyer et al. (2007).

*2.3.1.1 Eigenvalue decomposition* At every crank angle position, we record $N$ independent velocity fields during successive engine cycles, the so-called snapshots ($U^n$). Each snapshot consists of $m$ 2D velocity vectors. Phase-dependent POD, as the name suggests, calculates the POD modes for every specific CAD. The components $u$ and $v$ in $x$ and $y$ directions of each velocity vector ($u$, $v$) for each measured velocity field are stored in a velocity matrix, $\mathbf{U}$, in which each column represents one measured velocity field taken at the same crank angle, hence

$$\mathbf{U} = [U^1 U^2 \ldots U^N] = \begin{pmatrix} u_1^1 u_1^2 & \ldots & u_1^N \\ \vdots & \vdots & \vdots \\ u_m^1 & u_m^2 & \ldots & u_m^N \\ v_1^1 & v_1^2 & \ldots & v_1^N \\ \vdots & \vdots & \vdots \\ v_m^1 & v_m^2 & \ldots & v_m^N \end{pmatrix}. \quad (1)$$

Using the velocity matrix, the $N \times N$ space correlation matrix, or autocovariance matrix, is defined as:

$$\mathrm{R} = \mathbf{U}^{\mathrm{T}}\mathbf{U}, \quad (2)$$

for which the eigenvalue problem can be written as

$$\mathrm{RA} = \Lambda\mathrm{A}. \quad (3)$$

The eigenvalues ($\lambda$) from the eigenvalue array $\Lambda$ are then sorted in decreasing order: $\lambda_1 > \lambda_2 > \ldots > \lambda_N$. The eigenvectors ($\mathrm{A}_i$) are sorted in the same order as the eigenvalues and stored as a matrix used to define the POD mode matrix ($\Phi$) which is normalized:

$$\Phi = \frac{A\mathbf{U}}{\|A\mathbf{U}\|}. \quad (4)$$

The POD coefficients ($a$) for a specific snapshot are determined by projecting the velocity field of the snapshot onto the POD modes $\Phi$:

$$a_i^n = \Phi^i U^n. \quad (5)$$

Using the POD coefficients and the POD modes, a snapshot ($n$) can be reconstructed (subscript $r$) using:

$$U_r^n = \sum_{i=1}^{i_{max}} a_i^n \Phi^i. \quad (6)$$

When all POD mode contributions are included ($i_{\max} = N$), the snapshot is fully reconstructed.

For phase-invariant POD, all snapshots are stored in one single matrix **U**, the resulting number of columns is the product of the number of cycles and the number of visualized CAD positions. The subsequent eigenvalue decomposition procedure is the same as for phase-dependent POD. The number of POD modes resulting from this approach again equals the number of columns of **U**.

#### 2.3.2 Coordinate definition

In almost all flow research in engines conducted with PIV, the coordinate system is cartesian. However, when investigating the injection of a fuel spray in the swirl plane of a combustion engine, in which there is rotational symmetry in both flow and geometry, transforming the velocity information onto a polar grid, as done by Petersen and Miles (2011), can be expected to give more insight. By representing the data in radial and azimuthal directions, the influence of a radial injection of fuel on the dominantly azimuthal swirl can be investigated in more detail. The center point of the polar grid is positioned in the center of the combustion chamber, directly below the injector tip. An offset in swirl center position is not taken into account in this investigation, although the swirl center is not necessarily positioned in the center (see Zegers et al. 2009).

#### 2.3.3 Fluctuation definition

To investigate fluctuations, the turbulent kinetic energy (TKE) and its dissipation rate are often calculated from the 2D datasets, as shown by Saarenrinne and Piirto (2000), Müller et al. (2010) and Druault et al. (2005). By calculating the specific kinetic energy, the in-plane influence of the fuel injection on the flow is investigated as explained by Adrian et al. (2000). However, when the fluctuations are of the same order of magnitude as the mean velocity, it is more convenient to define the fluctuations ($u'$) as the Reynolds-decomposed part of the velocity. In this approach, the ensemble-averaged velocity field ($\overline{U}$) is subtracted from the instantaneous velocity fields ($U$), that is

$$u' = \frac{1}{m^2}\sum_{i,j=1}^{m}\frac{1}{N}\sum_{k=1}^{N}|U(i,j,k) - \overline{U}(i,j)|, \tag{7}$$

where $i$ and $j$ are the $r$- and $\theta$-components, respectively, and $k$ is the number of cycles. The results represent only two components of the velocity. The third component, in the vertical direction $z$, is not measured in this setup.

## 3 Results

The seeding material of hollow microspheres shows good laser scattering due to their large size, which can be seen in the PIV images in Fig. 3a, b. We observe no significant change of the microsphere size during the compression stroke. The heating effect and the increasing pressure seem to roughly cancel out, resulting in microspheres of almost constant size. The injection of fuel does not seem to affect the microspheres through the whole compression and work strokes of the engine. The region of bright scattering by the liquid fuel (Fig. 3b) is longer than would be expected on the basis of the geometrical overlap of the 1-mm-thick light sheet and the spray (see Fig. 2). This is probably due to multiple scattering. Inhomogeneities in the light sheet, partly due to obstruction by the fuel sprays, result in low signal levels in the lower left part of the images, resulting in low correlations in those areas and relatively many rejected vectors.

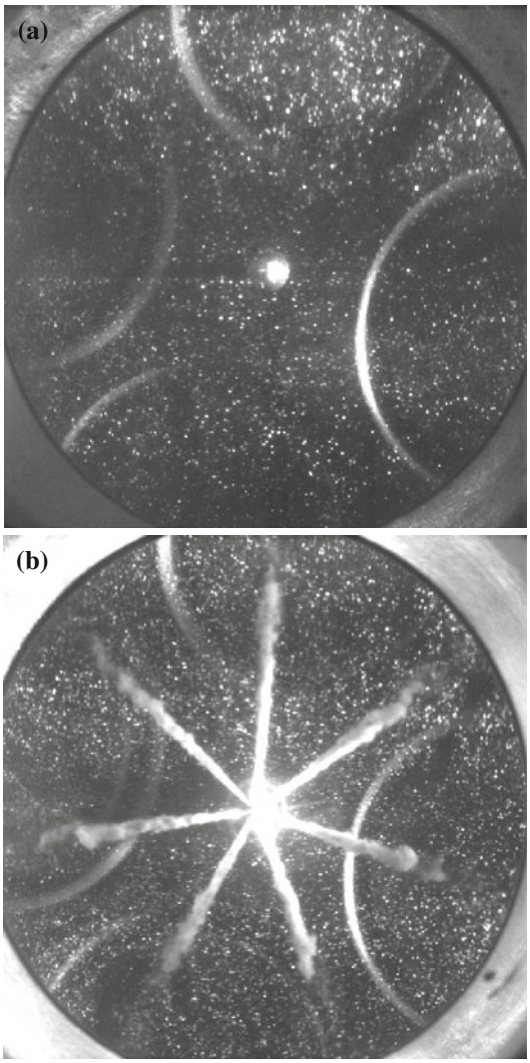


**Fig. 3** PIV images. **a** Representative camera image without fuel injection. **b** Representative camera image during spray injection around 330 CAD and $P_{\text{fuel}} = 2{,}500$ bar

### 3.1 Dataset 1: No injection

A typical instantaneous velocity field (snapshot) is shown in Fig. 4a. Averaging 310 velocity fields, all recorded at 329 CAD, results in the ensemble-averaged velocity field

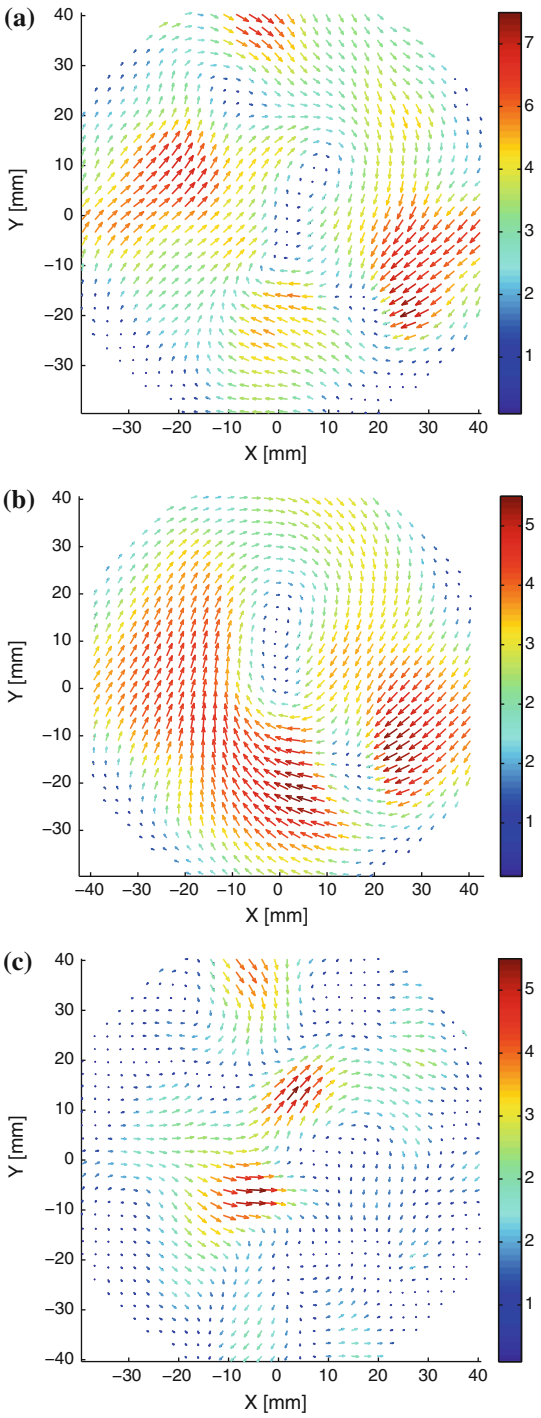


**Fig. 4** Typical velocity fields in (m/s) at 329 CAD (dataset 1). **a** Instantaneous velocity field CAD. **b** Ensemble-averaged velocity flow field. **c** Reynolds-decomposed velocity field

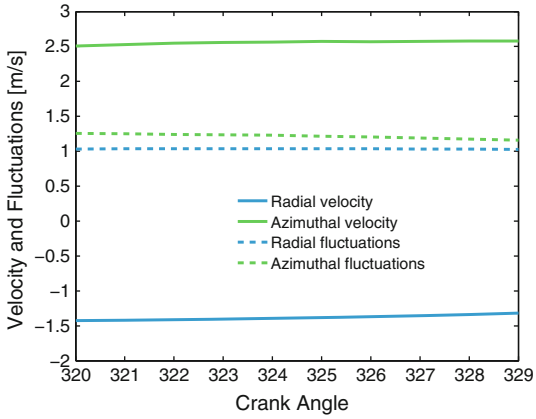


**Fig. 5** Spatially averaged velocity in $r$ and $\theta$ directions of 310 cycles as a function of crank angle position with an inlet pressure of 1 bar

of Fig. 4b. Note that the swirl center is slightly positioned off the central axis of the cylinder. This behavior was also observed previously by Zegers et al. (2009) in the same engine. Reynolds decomposition of the snapshot in Fig. 4a results in the fluctuation field presented by Fig. 4c. The kinetic energy contained in this residual velocity field is still 25 % of the energy present in the ensemble-averaged velocity field of Fig. 4b. This procedure was repeated for the complete dataset, and by spatially averaging the velocities and their corresponding fluctuations in radial and azimuthal directions, the evolution as a function of crank angle degree can be determined as depicted in Fig. 5. From this figure, it can be seen that the azimuthal and radial velocity components can be considered to be relatively stable, only showing small deviations over the investigated crank angle range. The radial component is negative, which means the flow is directed toward the center, due to squish motion. The azimuthal velocity component outweighs the radial component in absolute value, which is obvious when considering the swirl motion present in the instantaneous velocity fields. The fluctuations in azimuthal and radial directions are comparable in magnitude.

#### *3.1.1 Phase-dependent and phase-invariant POD analysis*

Using phase-dependent POD, the dataset of 310 snapshots is used to investigate the dominant flow structures, which contain the highest kinetic energy. When using the first mode to reconstruct an instantaneous velocity field, only the most dominant structures are present. An example is shown in Fig. 6a for the same instantaneous velocity field as given in Fig. 4a. This reconstruction contains 83 % of the energy present in the original velocity field and is the same as the ensemble-averaged velocity field. This is confirmed by plotting the difference between the two in Fig. 6b. By scaling the vectors, the swirling motion is still

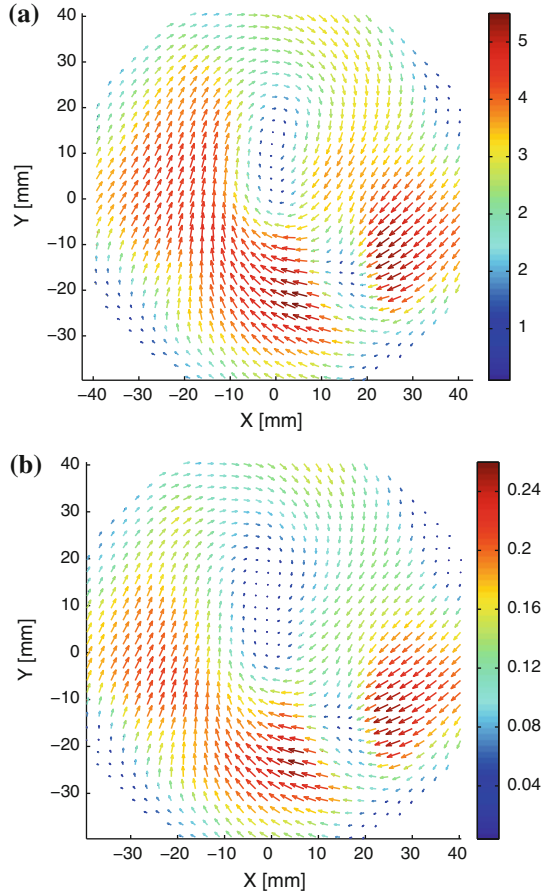


**Fig. 6** Reconstructed velocity field (m/s) and the corresponding residue. Note the difference in velocity scales. **a** Reconstructed snapshot of an instantaneous flow field at 329 CAD (Fig. 4a) using only the first mode. The reconstruction contains 83 % of the energy of the original snapshot. **b** Residue when subtracting the mean velocity field from the reconstructed snapshot using only the first mode of the flow field at 329 CAD. The residue contains only 0.2 of the energy in the ensemble-averaged velocity field

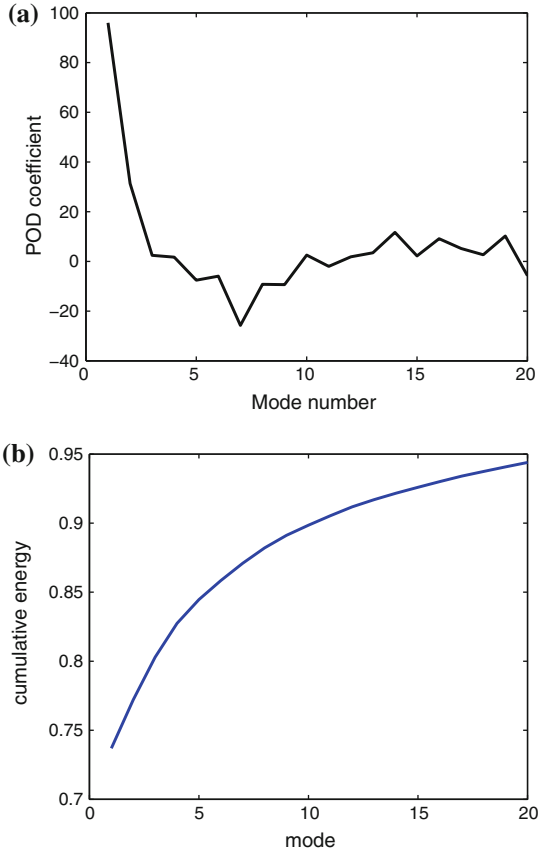


**Fig. 7** First 20 phase-dependent POD modes of the instantaneous flow field at 329 CAD as displayed in Fig. 4a. **a** POD coefficients. **b** Cumulative energy

noticeable; the velocities are however in the order of 0.2 m/s and represent only 0.2 % of the energy from the ensemble-averaged field. This is because the average velocity is not subtracted from the velocity field before starting the eigenvalue decomposition. However, the ensemble-averaged velocity field will differ significantly from the first mode if a large number of POD modes are required to capture a significant fraction of the flow's kinetic energy as presented by Liu and Haworth (2011).

The dominance of the first mode is clearly displayed in Fig. 7a, b where the POD coefficients and the cumulative energy are displayed for the first 20 modes. When applying phase-invariant POD using the complete crank angle range (3,100 snapshots), the resulting cumulative energy plot overlaps the line in Fig. 7b exactly and is therefore not shown. From this, we conclude that, for the case with 310 snapshots without fuel injection, there is no need to apply the phase-invariant POD to represent the instantaneous velocity fields as the energy represented by the same modes is equal for phase-dependent and phase-invariant POD.

### 3.2 Dataset 2: Fuel injections

Fuel has been injected at an increased inlet pressure of 2 bar. Eight cases without injection up to 330 CAD (Table 3; cases 1, 2, 4–8 and 10) were combined resulting in 72 cycles for crank angles up to 330 CAD. The corresponding spatially averaged velocities and fluctuations are depicted in Fig. 8. This figure clearly shows increasing azimuthal and radial velocities, whereas the fluctuations are relatively stable. The increase of in-plane velocities toward top dead center has been shown before by Zegers et al. (2009). The increase in the radial velocity toward the center (negative direction) can be attributed to the increase of squish motion between the piston and the cylinder head. The increase in azimuthal velocity depicts the increase in swirl motion, which can be ascribed to the conservation of angular momentum in a smaller volume due to compression. Comparing the crank angle range (320–329 CAD) of Fig. 5 with the same range in Fig. 8, it appears that velocities and fluctuations are similar.

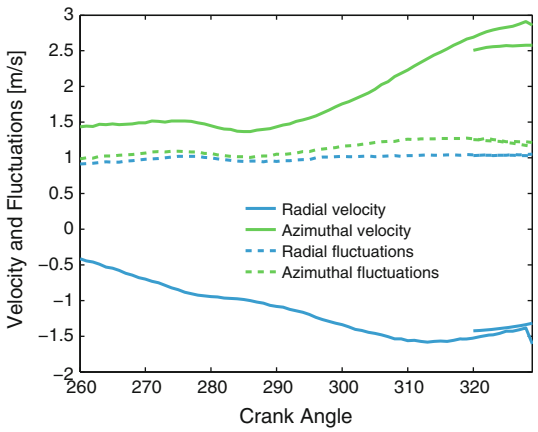


**Fig. 8** Spatially averaged velocities and fluctuations in $r$ and $\theta$ directions of 72 cycles as function of CA at 2 bar inlet pressure. The information from Fig. 5 (at 1 bar) has been plotted as well (320–329 CAD)

We conclude that the increased density, due to the increase in inlet pressure for dataset 2, does not have an important influence on the velocities.

### *3.2.1 Typical flow fields during injection*

A typical PIV image during injection is shown in Fig. 3b. Averaged flow fields for a double injection at 330 and 340 CAD (case 8) are shown in Fig. 9. Start of the first actuation is at 330 CAD, the injection starts around 331 CAD and ends 2 ms later around 337 CAD. The second injection starts around 341 CAD. During the initial phase, the flow of the injection (Fig. 9a) shows a distinct motion toward the center of the cylinder, due to air entrainment near the foot of the spray. Note that none of the velocity fields show the outward motion of the spray. This motion is not captured because the illuminated spray is almost completely removed from the recording during pre-processing. Vectors are displayed at positions of the fuel spray because the large 64 pixels interrogation windows use the surrounding displacement to calculate the displacement at those positions, and for the same reason, the outward velocity of the regions near the spray is not captured. The largest bias errors therefore occur at the spray positions and its near surrounding as shown in Fig. 3b. Moreover, the combination of the 50-µsec pulse separation and the 1-mm thin laser sheet biases our measurements to structures with axial velocities $V_z < 20$ m/s. The speed of the fuel spray is in the order of 200 m/s and will induce a large out-of-plane motion.

After 7 CAD of injection, the flow behavior has changed into a less coherent motion, as shown in Fig. 9b. The air entrainment from below the spray (indicated by the green

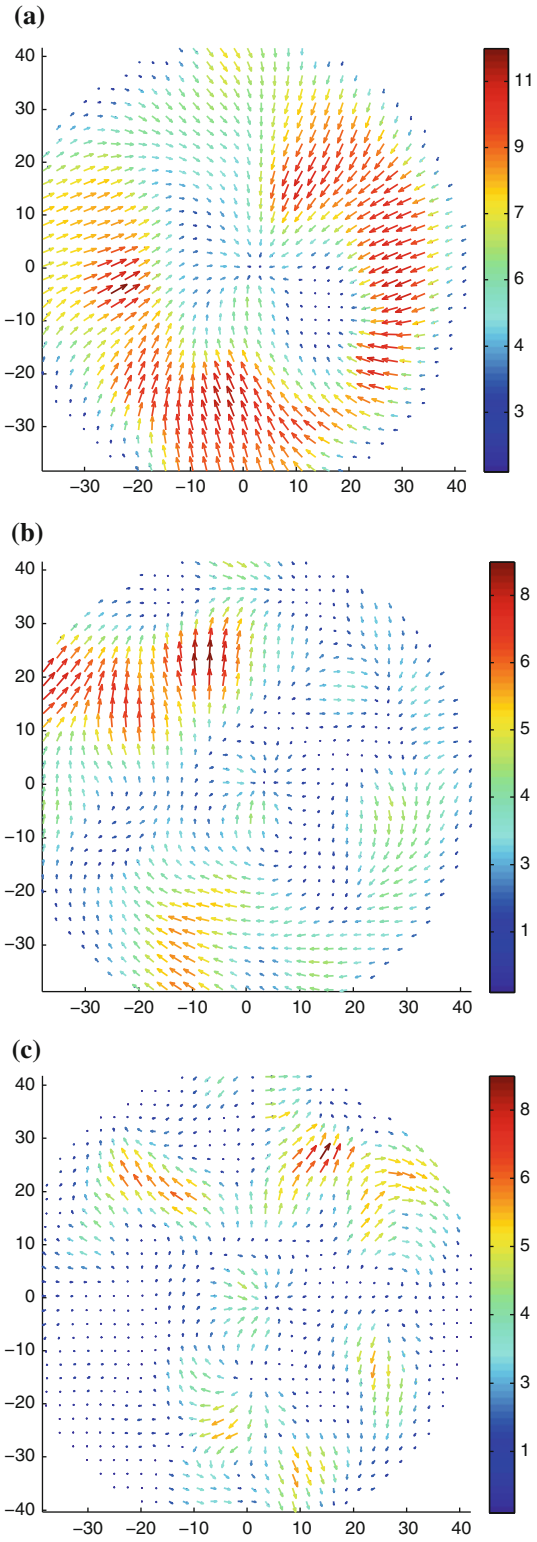


**Fig. 9** Ensemble-averaged velocity fields (m/s) for case 8 with a 2-ms double fuel injection at 330 and 340 CAD and 2,500 bar injection pressure. **a** 333 CAD (during first injection). **b** 337 CAD (end of first injection). **c** 345 CAD (during second injection)

arrow in Fig. 10a) leads to a positive outward motion. Combined with a significant amount of induced out-of-plane motion, the resulting velocity field recorded has very low averaged velocities between 337 and 340 CAD, when the second injection starts.

The inward motion due to air entrainment during the second injection at 345 CAD (Fig. 9c) is strongly influenced by other flow structures present, possibly by the re-entrance of the first injection via impingement on the piston and cylinder, as illustrated by the pink arrow in Fig. 10a or by the entrainment from below.

The influence of injection timing and injection pressure on the flow field is addressed in more detail in the next subsections.

### 3.2.2 *Influences of injection timing*

The piston position as function of CAD is illustrated in Fig. 10. Upon injection at crank angle degrees between 350 and 370, the fuel will be directed into the piston bowl as visualized in Fig. 10b. For all other crank angles, the fuel does not impinge on the piston bowl wall and enters the squish region above the bowl ring (Fig. 10a). The position of the fuel impingement appears crucial for the flow development inside the cylinder.

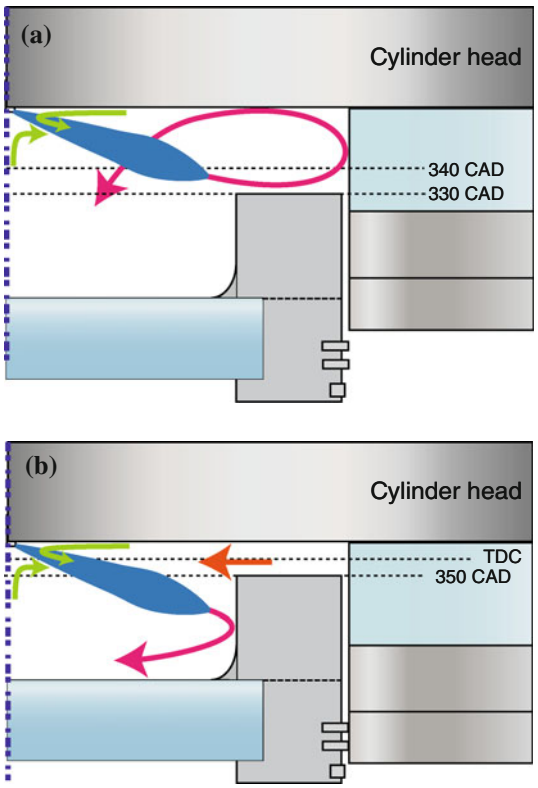


**Fig. 10** Schematic representation at two different CAD of the fuel injection and the corresponding major fuel flow patterns (*pink*), squish motion (*orange*) and entrainment motion (*green*). **a** Injection before 350 CAD. **b** Injection after 350 CAD

The influence of the injections on the flow field has been investigated by averaging the spatially averaged velocity fields for each crank angle degree in $r$ and $\theta$ directions separately. The same has been done for the corresponding fluctuations. Several cases have been combined in Figs. 11, 12, 13, 14.

Injection timing was varied from 330 CAD to 350 CAD with constant injection pressure (cases 6, 7, 8 and 10); the results for the spatially averaged velocities and their fluctuations are shown in Figs. 11 and 12. Within each figure, the curves are similar, but shifted in time following the injection timing, showing smaller velocities and fluctuations for the cases with a retarded injection timing. These differences can be explained by the influence of the different piston position and a corresponding change in flow behavior, where the piston position at later injection timings significantly dampens the radial motion.

Pronounced peaks toward negative radial velocity are observed for each injection, indicative for air entrainment (Figs. 11a, 12a). After each injection, the radial velocity values switch from negative to positive, which can be attributed to the entrainment wave as observed by Musculus and Kattke (2009).

For later injection timings, the average radial velocity during injection is close to zero, indicating a balance between entrainment and outward directed flow structures. At the beginning of each injection, during air entrainment, radial fluctuations are relatively small, rising steeply near the end of the injection as depicted in Figs. 11c and 12c. The average azimuthal velocities drop sharply only at the end of the (first) injection, and simultaneously its fluctuations rise (Fig. 11d).

### 3.2.3 *Influences of injection pressure*

Injection pressure was increased for the same injection timings from 2,000 to 2,500 bar (cases 3 and 11, Fig. 13) and from 1,500 to 2,500 bar (cases 1,4 and 5, Fig. 14). An increase in injection pressure does not seem to lead to increased velocities (Fig. 13), the fluctuations do not correlate very well with injection pressure.

Figure 14 does show variations in the integrated flow field with changing injection pressure, but does not show a clear trend. This is not to be expected from momentum conservation and might be related to different injector behavior when fuel pressure is changed and a different mass flow. Further research should be performed to investigate how increasing injection pressure, and therefore increasing fuel momentum, influences the flow fields inside the piston bowl.

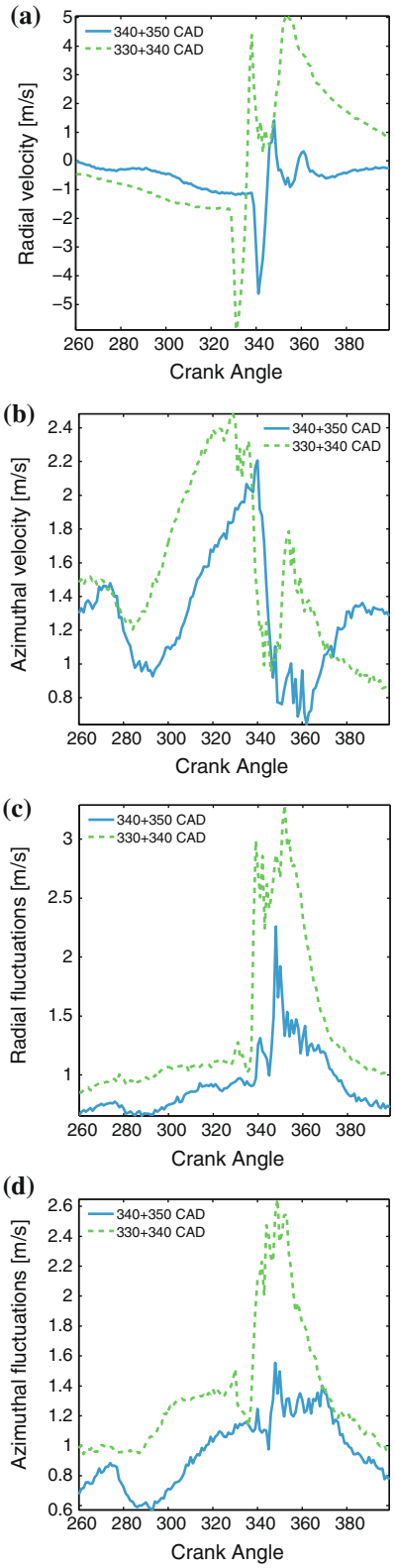


**Fig. 11** Spatially averaged velocity and corresponding fluctuations in $r$ and $\theta$ directions of cases 7 and 8. Fuel was injected at 330 and 340 CAD respectively 340 and 350 CAD with 2,500 bar injection pressure and injection durations of 2 ms. **a** Radial velocity. **b** Azimuthal velocity. **c** Radial fluctuations. **d** Azimuthal fluctuations

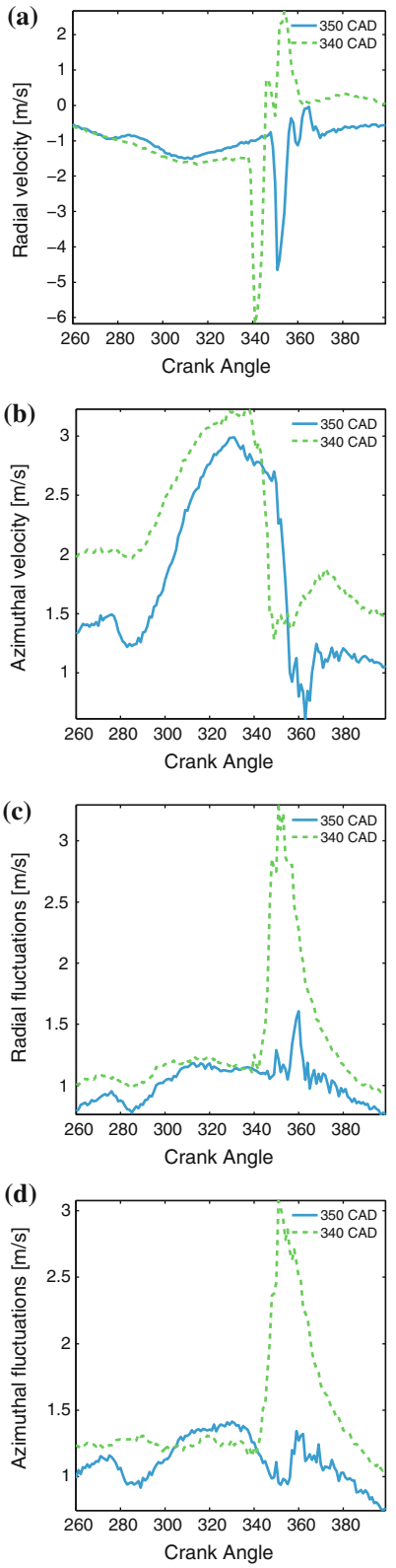


**Fig. 12** Spatially averaged velocity and corresponding fluctuations in $r$ and $\theta$ directions of cases 6 and 10. Fuel was injected at 340 respectively 350 CAD with 2,500 bar injection pressure and injection durations of 3 s. **a** Radial velocity. **b** Azimuthal velocity. **c** Radial fluctuations. **d** Azimuthal fluctuations

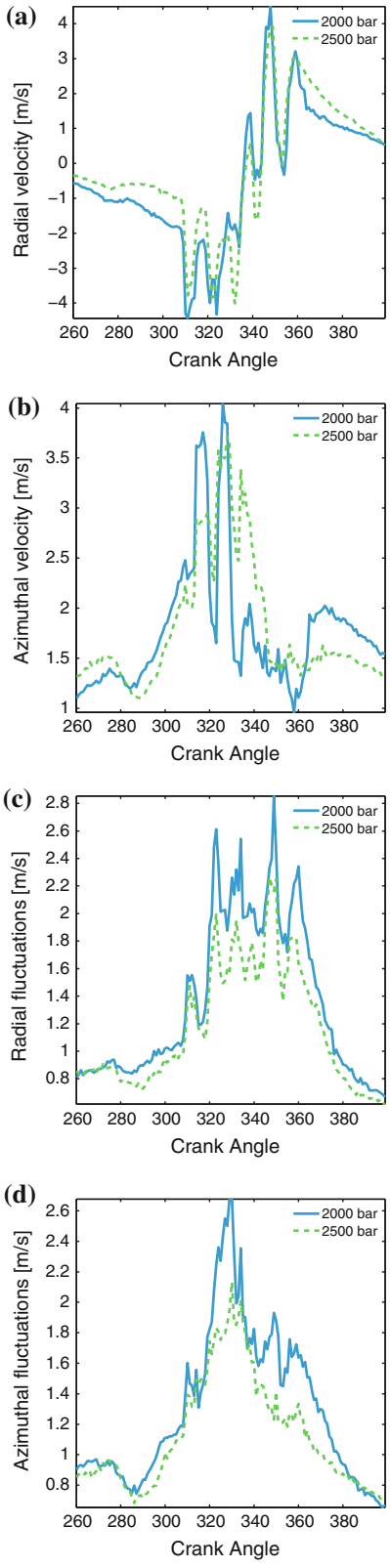


**Fig. 13** Spatially averaged velocity and corresponding fluctuations in $r$ and $\theta$ directions of cases 3 and 11. Fuel was injected at 310, 320, 330, 340 and 350 CAD, with injection durations of 1 s. **a** Radial velocity. **b** Azimuthal velocity. **c** Radial fluctuations. **d** Azimuthal fluctuations

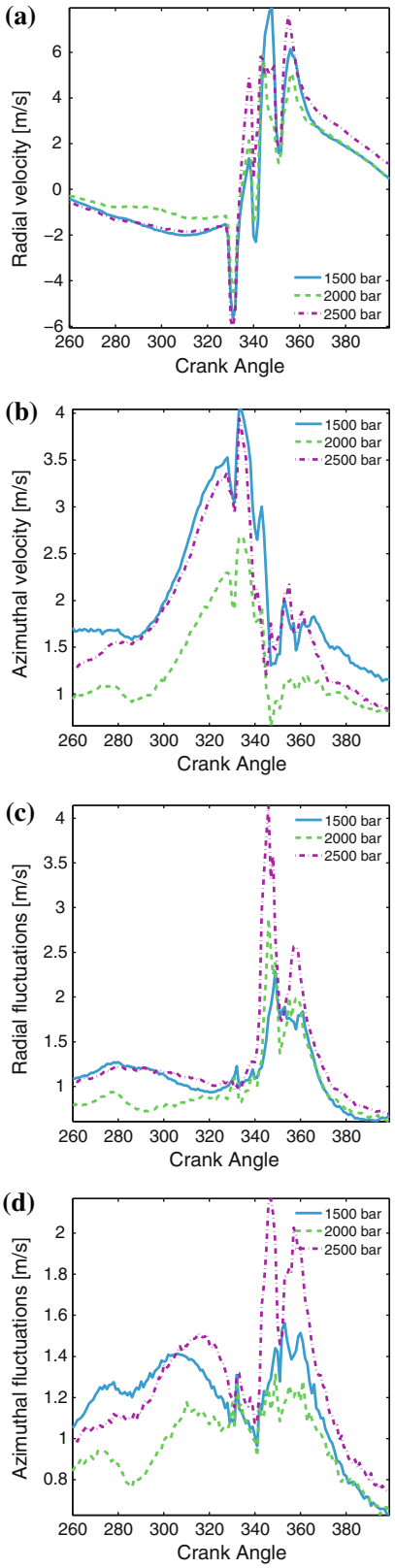


**Fig. 14** Spatially averaged velocity and corresponding fluctuations in $r$ and $\theta$ directions for cases 1, 4 and 5. Fuel was injected at 330, 340 and 350 CAD with injection durations of 1 ms. **a** Radial velocity. **b** Azimuthal velocity. **c** Radial fluctuations. **d** Azimuthal fluctuations

### 3.2.4 Phase-dependent POD analysis

Phase-dependent POD analysis is performed on a typical cycle from case 8. By doing so, there are only 9 modes. The POD coefficients for the most dominant modes are shown in Fig. 15a for the whole measurement span (260–400 CAD) and for a subrange (330–360 CAD) in Fig. 15b. In these figures, the dominance of the first mode is obvious before and during the first injection, but not during the second injection (340–348 CAD) when the first five modes are almost equally contributing to the instantaneous velocity fields. This indicates that, upon injection, the flow changes into an incoherent flow with unrelated structures in each snapshot. Immediately after the second injection, around 350 CAD, the POD coefficient of the first mode increases rapidly again, indicating a re-establishment of coherent flow. Averaging the POD coefficients over the 9 available cycles reduces the noise-like structures and results in Fig. 16. The drop in magnitude of the dominant POD coefficient during injection corresponds with the decrease in radial and azimuthal velocities around 340 CAD as shown in Fig. 11.

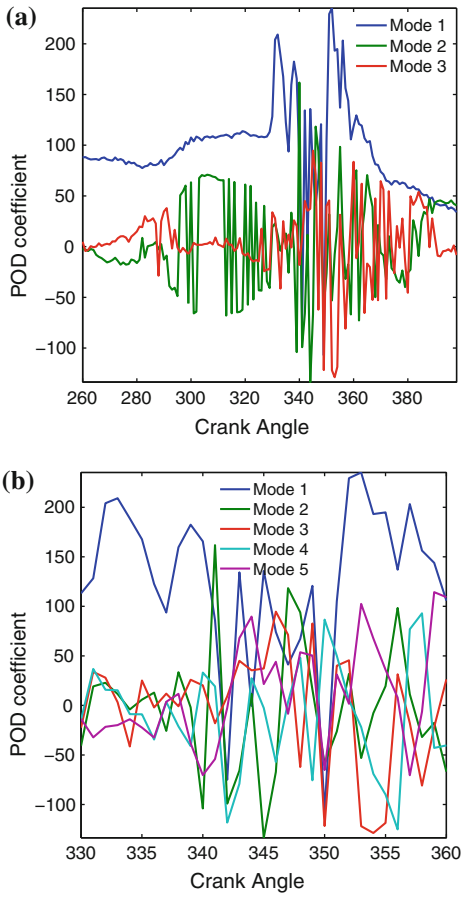


**Fig. 15** Phase-dependent POD analysis for a typical cycle from case 8. Fuel was injected at 330 and 340 CAD with durations of 2 ms. **a** POD coefficients ($a_i^n$) for modes 1–3. **b** POD coefficients ($a_i^n$) for modes 1–5

In Fig. 17, the normalized eigenvalues ($\lambda$) are shown for the accumulation of the first five modes of case 8. The dip in the eigenvalue of the first modes after 340 CAD supports the observed lack of coherent structures in Fig. 16b. For crank angles during the first injection starting at 330 CAD, the first mode contributes about 90 % to the total energy and drops a little bit until the second injection starts at 340 CAD. During and after the second injection, the energy present in the first mode drops to a level of 20 % and the first five modes combined only capture 75 % of the energy.

### 3.2.5 Phase-invariant POD analysis

To investigate whether POD modes from different crank angles can be used to represent the measured velocity fields during and after injection, phase-invariant POD has also been applied to case 8. There are no phase-dependent eigenvalues and eigenvectors any more, only the POD coefficients themselves can be studied to judge the dominance of certain modes. The results of the phase-invariant analysis are shown in Fig. 18. The fluctuations observed in the POD coefficients for one cycle in Fig. 18a are greatly reduced by averaging the POD coefficients for the 9 available cycles as shown in Fig. 18b. To interpret the results, a comparison is made with the phase-dependent POD. Contrary to the phase-dependent POD case given in Fig. 15, there is no clear dominance of a single mode, except, surprisingly, at the start of the first and of the second (last) injection. Apparently, these events are sufficiently violent to put a stamp on the global flow pattern even though they dominate the flow for just a few crank angle degrees. The lack of a single dominant mode is confirmed by Fig. 18c, showing that mode 1 contributes around 30 % to the total energy and mode 2 in the order of 20 % (Fig. 19).

The phase-invariant POD analysis can be applied to datasets with a low number of snapshots to increase the amount of data in the analysis. However, using snapshots of the flow fields without injection as a basis for flow fields at crank angle degrees after injection does not seem to be a good strategy for sets of data in which the injection of fuel changes the flow field drastically. Because of the lack of resemblance between flow fields, the use of separate basis functions for each crank angle seems more appropriate. Possibly, a more promising strategy could be to use two sets of base functions, one for the period before injection and one for the period after the start of the first injection.

What can be learned from the performed POD analysis is the lack of coherent structures during an injection. This can be seen from the sudden drop in POD coefficient of mode 1 and the rise of higher modes.

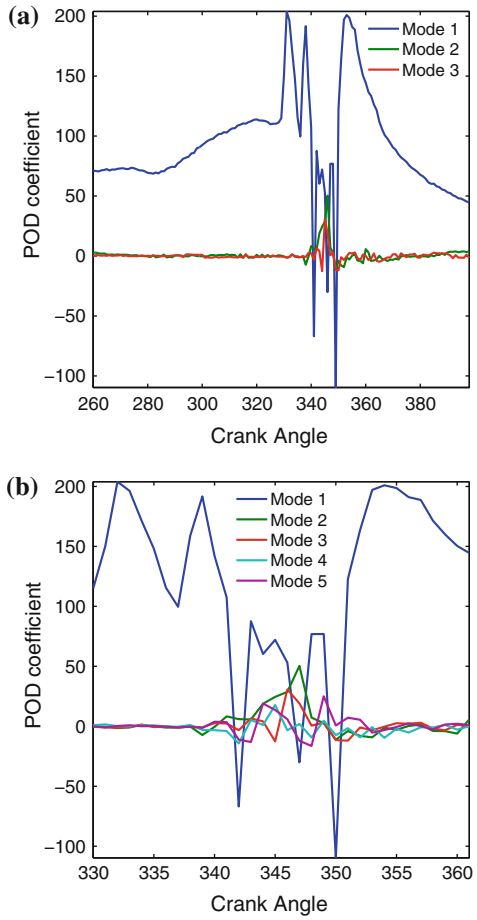


**Fig. 16** Averaged phase-dependent POD analysis for all cycles from case 8. Fuel was injected at 330 and 340 CAD with durations of 2 ms. **a** Averaged POD coefficients ($a_i$) for modes 1–3. **b** Averaged POD coefficients ($a_i$) for modes 1–5

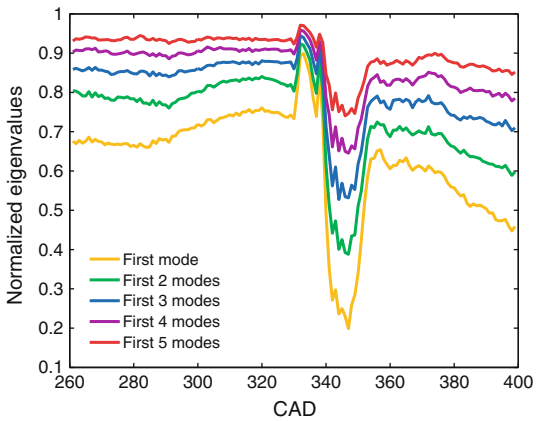


**Fig. 17** Normalized eigenvalues ($\lambda$) as function of CAD for the phase-dependent POD analysis for case 8. Fuel was injected at 330 and 340 CAD with durations of 2 s

## 4 Conclusions

In this study, the applicability of HS-PIV to investigate large in-cylinder flow structures during and after fuel injection has been proven. The hollow microspheres used as seeding material perform very well before, during and after injection.

At crank angles without fuel injection, velocity fluctuations are in the order of 50 % of the average absolute velocity. Increasing the inlet pressure and therefore density does not show an influence on the velocities and fluctuations for the invested crank angle range of 320–329 CAD. POD analysis shows that a snapshot reconstruction using only the first mode differs only 0.2 % in energy from the ensemble-averaged velocity field.

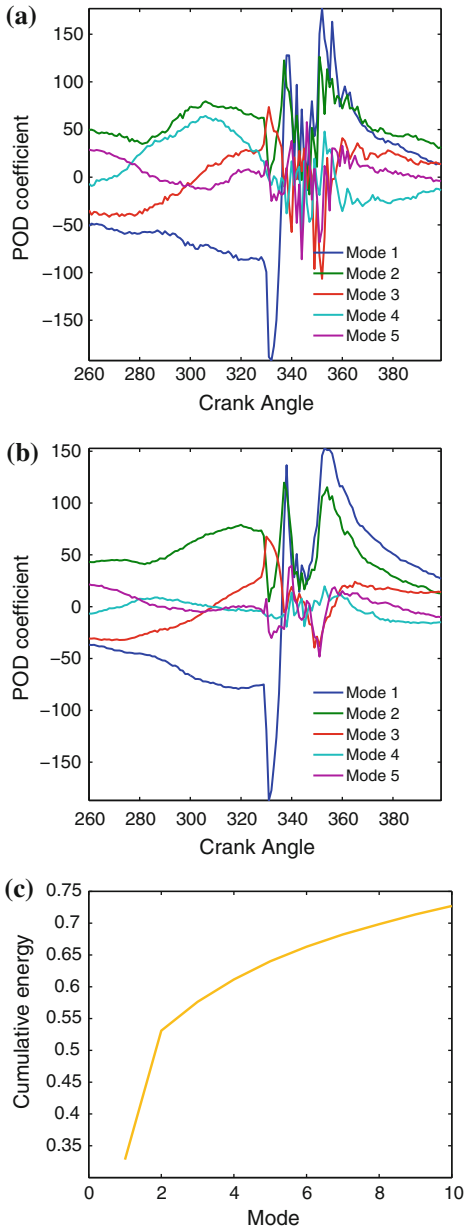


**Fig. 18** Phase-invariant POD analysis of case 8. Fuel was injected at 330 and 340 CAD with durations of 2 ms. **a** POD coefficients ($a_i^n$) of cycle 1 for modes 1–5. **b** Averaged POD coefficients of 9 cycles ($a_i$) for modes 1–5. **c** Cumulative energy

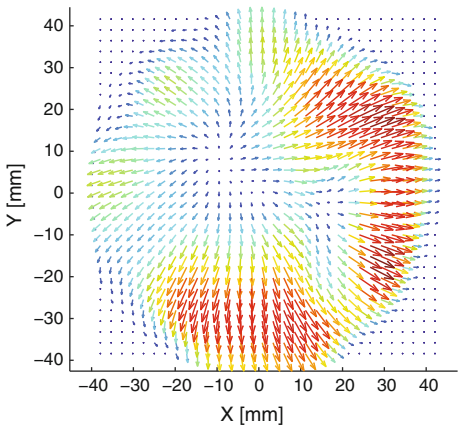


**Fig. 19** Mode 1 of the phase-invariant POD for case 8

During injection of fuel, air entrainment is observed, witnessed by a strong increase of the in-plane velocity and the corresponding fluctuations during the injection event. In the case of multiple injections, the air entrainment during the first injection is consistent and the fluctuations between consecutive cycles small. When previous injections re-enter the investigated plane via impingement on the wall or top of the piston, the in-plane structures change drastically into less coherent structures, compensating the inward motion due to air entrainment by subsequent injections. The spray-induced flow can evolve in different structures, which might influence the actual mixing of fuel and air, causing differences in fuel and air ratios between different injection strategies and therefore change the combustion delay present in PCCI combustion.

The applied POD analysis supports the observed changes in flow structures during and after injection and might be a good tool for comparison with future CFD results. For CAD with high fluctuations, as observed during injection, a good representation of the instantaneous velocity field using only a few POD modes is not possible.

Phase-invariant POD is not an appropriate method to represent highly fluctuating flows during and after fuel injections. Because of the lack of resemblance between crank angle degrees, the use of separate basis functions for each CAD is more appropriate; alternatively, one could use separate sets of base functions before and during injection.

Restricting the investigated crank angle range and therefore enabling the recording of more velocity fields during the ignition delay period increase the amount of snapshots for the POD analysis and increase measurement accuracy.

**Acknowledgments** The project "Towards clean diesel engines" was funded by the Dutch Technology Foundation STW. DAF Trucks N.V., Shell Global Solutions, Wärtsilä, TNO and Delphi Diesel Systems are also acknowledged for their contributions to the project.



## References

Adrian RJ, Christensen KT, Liu ZC (2000) Analysis and interpretation of instantaneous turbulent velocity fields. Exp Fluids 29:275–290

Bizon K, Continillo G, Leistner K, Mancaruso E, Vaglieco BM (2009) POD-based analysis of cycle-to-cyle variations in an optically accessible diesel engine. Proc Combust Inst 32:2809–2816

Bizon K, Continillo G, Mancaruso E, Merola SS, Vaglieco BM (2010) POD-based analysis of combustion images in optically accessible engines. Combust Flame 157:632–640

Chartier C, Andersson O, Johansson B, Musculus M, Bobba M (2011) Effects of post-injection strategies on near-injector over-lean mixtures and unburned hydrocarbon emission in a heavy-duty optical diesel engine. SAE Technical Paper 2011-01-1383

Chatterjee A (2000) An introduction to the proper orthogonal decomposition. Cur Sci 78(7):808–817

Cosadia I, Borée J, Charnay G, Dumont P (2006) Cyclic variations of the swirling flow in a diesel transparent engine. Exp Fluids 41:115–134

Cosadia I, Borée J, Dumont P (2007) Coupling time-resolved PIV flow-fields and phase-invariant proper orthogonal decomposition for the description of the parameter space in a transparent diesel engine. Exp Fluids 43:357–370

Dempsey AB, Reitz RD (2011) Computational optimization of a heavy-duty compression ignition engine fueled with conventional gasoline. SAE Technical Paper 2011-01-0356

Doosje E (2010) Limits of mixture dilution in gas engines. PhD thesis, Eindhoven University of Technology

Druault P, Guibert P, Alizon F (2005) Use of proper orthogonal decomposition for time interpolation from PIV data - application to the cycle-to-cycle variation analysis of in-cylinder flows. Exp Fluids 39:1009–1023

Ekenberg M, Reinmann R, Olofsson E, Gillet B, Johansson B (2001) The influence of a late in-cylinder air injection on in-cylinder flow measured with particle image velocimetry (PIV). SAE Technical Paper 2001-01-3492

Hillamo H, Kaario O, Larmi M (2008) Particle image velocimetry measurements of a diesel spray. SAE Technical Paper 2008-01-0942

Hillamo H, Anttinen T, Aronsson U, Chartier C, Andersson Ö, Johansson B (2011) Flow field measurements inside a piston bowl of a heavy-duty diesel engine. SAE Technical Paper 2011-01-1835

Krishna BM, Mallikarjuna JM (2010) Comparative study of in-cylinder tumble flows in an internal combustion engine using different piston shapes an insight using particle image velocimetry. Exp Fluids 48:863–874

Leermakers CAJ, Luijten CCM, Somers LMT, Kalghatgi GT, Albrecht BA (2011) Experimental study of fuel composition impact on PCCI combustion in a heavy-duty diesel engine. SAE Technical Paper 2011-01-1351

Liu K, Haworth DC (2011) Development and assessment of POD for analysis of turbulent flow in piston engines. SAE Technical Paper 2011-01-0830

Malbec LM, Bruneaux G (2010) Study of air entrainment of multi-hole diesel injection by particle image velocimetry - effect of

neighboring jets interaction and transient behaviour after end of injection. SAE Technical Paper 2010-01-0342

Melling A (1997) Tracer particles and seeding for particle image velocimetry. Meas Sci Tech 8(12):1406

Meyer KE, Cavar D, Pedersen JM (2007) POD as tool for comparison of PIV and LES data. In: 7th international symposium on particle image velocimetry, Rome, Italy

Müller SHR, Böhm B, Gleißner M, Grzeszik R, Arndt S, Dreizler A (2010) Flow field measurements in an optically accessible, direct-injection spray-guided internal combustion engine using high-speed PIV. Exp Fluids 48:281–290

Musculus MPB, Kattke K (2009) Entrainment waves in diesel jets. SAE Int J Engines 2:1170–1193

Nordgren H, Hildingsson L, Johansson B, Dahlén L, Konstanzer D (2003) Comparison between in-cylinder PIV measurements, CFD simulations and steady-flow impulse torque swirl meter measurements. SAE Technical Paper 2003-01-3147

Petersen B, Miles P (2011) PIV measurements in the swirl-plane of a motored light-duty diesel engine. SAE Int J Engines 2011-01-1285

Peterson B, Sick V (2009) Simultaneous flow field and fuel concentration imaging at 4.8 kHz in an operating engine. Appl Phys B 97:887–895

Raffel M, Willert CE, Wereley ST, Kompenhans J (2007) Particle image velocimetry—a practical guide. Springer, Berlin

Roudnitzky S, Druault P, Guibert P (2006) Proper orthogonal decomposition of in-cylinder engine flow into mean component, coherent structures and random gaussian fluctuations. J Turb 7:N70

Saarenrinne P, Piirto M (2000) Turbulent kinetic enregy dissipation rate estimation from PIV velocity vector fields. Exp Fluids S300–S307

Sirovich L (1987) Turbulence amd the dynamics of coherent structures, part I: coherent structures. Q Appl Math XLV: 561–571

Towers DP, Towers CE (2004) Cyclic variability measurements of in-cylinder engine flows using high-speed particle image velocimetry. Meas Sci Technol 15:1917–1925

Yu R, Bai XS, Hildingsson L, Hultqvist A, Miles P (2006) Numerical and experimental investigation of turbulent flows in a diesel engine. SAE Technical Paper 2006-01-3436

Zegers RPC, Meyden TJvd, Luijten CCM, Dam NJ, Baert RSG, Goey LPHd (2009) Crank angle resolved flow field characterization of a heavy-duty (PCCI) engine. In: Proceedings of the European Combustion Meeting